Multiferroic Two-Dimensional Materials

L. Seixas,[1,2,*] A. S. Rodin,[1] A. Carvalho,[1] and A. H. Castro Neto[1]
[1]*Centre for Advanced 2D Materials and Graphene Research Centre, National University of Singapore, Singapore 117542, Singapore*
[2]*MackGraphe—Graphene and Nanomaterials Research Center, Mackenzie Presbyterian University, 01302-907 São Paulo, São Paulo, Brazil*

(Received 30 October 2015; published 20 May 2016)

The relation between unusual Mexican-hat band dispersion, ferromagnetism, and ferroelasticity is investigated using a combination of analytical, first-principles, and phenomenological methods. The class of material with Mexican-hat band edge is studied using the α-SnO monolayer as a prototype. Such a band edge causes a van Hove singularity diverging with $1/\sqrt{E}$, and a charge doping in these bands can lead to time-reversal symmetry breaking. Herein, we show that a material with Mexican-hat band dispersion, α-SnO, can be ferroelastic or paraelastic depending on the number of layers. Also, an unexpected multiferroic phase is obtained in a range of hole density for which the material presents ferromagnetism and ferroelasticity simultaneously.

DOI: 10.1103/PhysRevLett.116.206803

Recently, a number of two-dimensional (2D) materials have been found to exhibit band dispersions unrelated to their parent three-dimensional (3D) materials. Some curious example are the materials with a Mexican-hat band which results in van Hove singularities (VHSs) with $1/\sqrt{E}$ divergence in the density of states (DOS). This novel material class includes gallium or indium monochalcogenides [1–3], and bilayer graphene under an electric field [4–7]. This leads to an electronic instability, often resulting in magnetism, distortion with spatial symmetry breaking, or superconductivity.

First-principles calculations show that GaS [3] and GaSe [2,3] monolayers become ferromagnetic when hole doped. Here, we demonstrate that this finding is general for materials with Mexican-hat band edges (MHBEs). In addition, we show that ferromagnetism and ferroelasticity not only may arise in 2D materials with MHBE, but that both ferroic orders may even be stable simultaneously.

This multiferroicity offers a promising approach to achieve controllable ferromagnetism in 2D materials, where the doping density can be varied by external gating. In fact, most attempts so far to achieve magnetism in 2D have made use of magnetic atoms [8,9], edges [10,11], or other defects [12,13]. However, these modified materials have been difficult to synthesize and characterize experimentally, and are far from controllable. In contrast, in materials with Mexican-hat–like bands, magnetism is inherent. Thus, this class of magnetic materials stands apart within 2D crystals, and may well become the much sought-after monolayer ferromagnetic element needed for designing fully 2D spintronic devices, with the added advantage of allowing for electrical and mechanical tuning of the magnetic state.

Herein, we investigate the relation between Mexican-hat band edges, ferromagnetism, and ferroelasticity. As a prototype of this phenomenon, we use p-doped α-SnO, in which ferroelastic and ferromagnetic orders coexist.

Mexican-hat bands are described by

$$E(k) = Ak^4 + Bk^2 + E_0, \tag{1}$$

where $k = |\mathbf{k}|$ refers to a point of the reciprocal space. The A and B constants are: $A < 0$ and $B > 0$ for the valence band edge, or $A > 0$ and $B < 0$ for the conduction band edge. The hat depth, E_0, is defined as the energy difference between the local band extrema. This kind of band edge is shown schematically in Fig. 1(a) for $A > 0$ and $B < 0$. The MHBEs have global extrema in an annular region with radius $k_0 = \sqrt{-B/(2A)}$, and local extrema at the Γ point. Setting the annular band extrema to zero, the hat depth becomes $E_0 = B^2/4A$. These bands possess two VHSs: (i) a divergence in the density of states (DOS) with $1/\sqrt{E}$ behavior at $E = 0$, (ii) a Heaviside step function

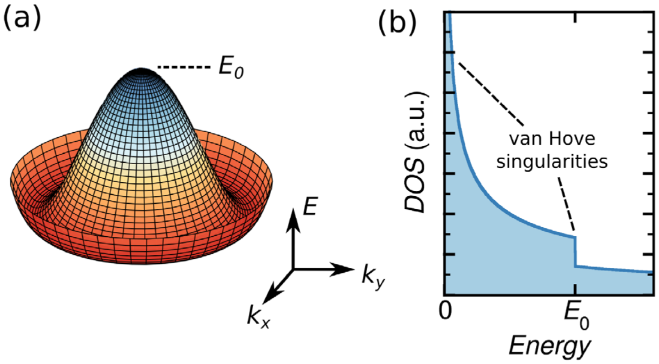

FIG. 1. Mexican-hat band edge model. (a) Schematic representation of a MHBE with depth E_0. (b) Density of states of two VHSs: One at $E = 0$ with $1/\sqrt{E}$ divergence, and another with Heaviside step function discontinuity at $E = E_0$.

discontinuity at $E = E_0$. Thus, the DOS for the MHBE is given by

$$\mathrm{DOS}(E) = \frac{1}{4\pi\sqrt{A}}\frac{1}{\sqrt{E}}\left[1 - \frac{\Theta(E - E_0)}{2}\right] \tag{2}$$

for the conduction band edge ($A > 0$). This DOS is shown in Fig. 1(b). Details of the calculation of this DOS are found in the Supplemental Material [14].

We use state-of-art first principles calculations based on density functional theory (DFT) [20,21] as implemented in the Vienna *ab initio* simulation package (VASP) [22,23]. The external potential is given by the projector augmented-wave (PAW) approximation [24], and the exchange-correlation functional is given by the generalized gradient approximation parameterized by Perdew, Burke, and Ernzerhof (GGA-PBE) [15] or the hybrid exchange-correlation functional parameterized by Heyd, Scuseria, and Ernzerhof (HSE06) [25]. The plane-wave basis with a kinetic energy cutoff of 800 eV is used in all first-principles calculations. The k-point samples in the Brillouin zone are calculated with the Γ-centered Monkhorst-Pack algorithm [26] with $15 \times 15 \times 1$ grid for monolayers and bilayers, and $15 \times 15 \times 10$ for bulk geometries. All geometries are relaxed until residual forces are smaller than 10^{-3} eV/Å, and using nonlocal van der Waals forces in the optB86b-vdW approximation [16,17]. We use a vacuum spacing of 20 Å along the z axis to avoid spurious interactions.

In order to study the consequences of the DOS divergence for a particular case, we consider monolayer α-SnO [27]. The crystal structure of a α-SnO monolayer has tetragonal symmetry, see Fig. 2(a). The oxygen atoms are arranged in a planar square sublattice, while the tin atoms form alternating pyramids with square bases bounded by the oxygen atoms [28–31]. Using first-principles calculations with van der Waals (vdW) forces, we find a lattice constant of $a_{1L} = 3.803$ Å for α-SnO monolayers. This lattice constant is slightly smaller than the one calculated for the bilayer and bulk, $a_{2L} = 3.820$ Å and $a_{\mathrm{bulk}} = 3.838$ Å, respectively. Comparisons of lattice constants with different parameterization and experimental values are shown in the Supplemental Material [14]. The α-SnO monolayer is an insulator with a fundamental indirect band gap of 3.93 eV at HSE06 level, as shown in Fig. 2(b). The optical band gap is about 4.00 eV at the Γ point, with the same exchange-correlation functional. In contrast, the α-SnO bulk is a semiconductor with a fundamental indirect band gap of 0.7 eV and optical band gap of 2.7 eV [30,32]. Since the valence band of the monolayer is a shallow MHBE at the Γ point, we expect an electronic instability via VHS.

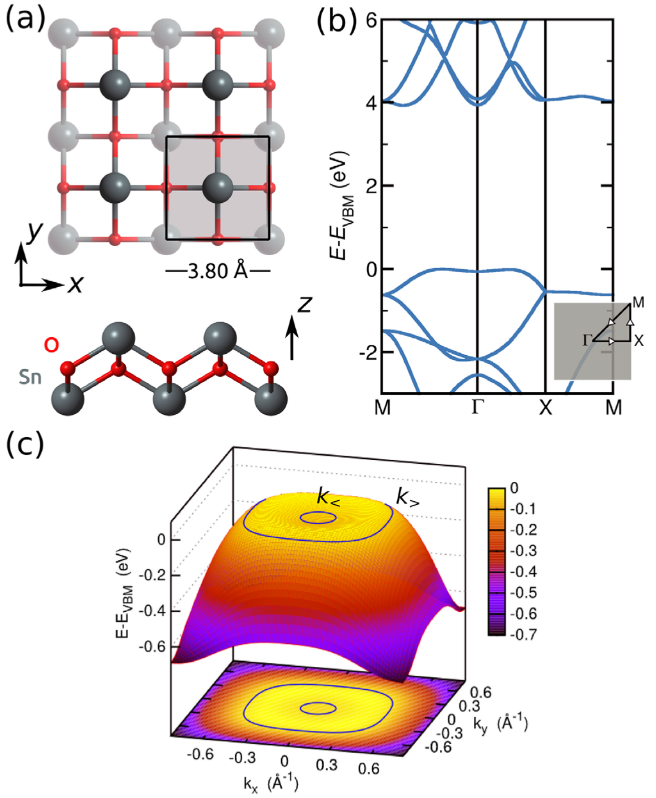

FIG. 2. α-SnO monolayer with tetragonal symmetry. (a) Ball-and-stick representation of the α-SnO monolayer from the top view (top panel) and side view (bottom panel). (b) First principles electronic band structure of the α-SnO monolayer at HSE06 level. (c) Mexican-hat valence band surface at PBE level. Contour lines at $E - E_{\mathrm{VBM}} = -0.030$ eV in the valence band are labeled by $k_<$ and $k_>$.

As an approximation, we can consider the valence band maxima as the annular region with radius k_0. For Fermi levels between the local band extrema, the Fermi surface is formed by two circular regions with radii $k_<$ and $k_>$, as shown in Fig. 2(c). For band structures calculated with HSE06, the Mexican-hat depth is $E_0^{\mathrm{HSE06}} = -0.052$ eV. With the PBE functional, the depth is $E_0^{\mathrm{PBE}} = -0.037$ eV. For Fermi levels lower than E_0, the Fermi surface is formed by only one ring with radius $k_>$. Note that with increasing radii $k_<$ and $k_>$, there is a tetragonal warping.

Thus, the most interesting situation to consider, aside from the intrinsic material, is the p-type material where the Fermi level lies close to the singularity. This is a realistic scenario, since previous studies of α-SnO bulk show that Sn vacancies are the most stable native defects [33]. These defects are acceptors, doping the α-SnO with holes. Furthermore, adding the 2D material in a device with an electrolyte gate, we can achieve carrier dopings up to 10^{15} cm^{-2} [34,35].

Given the high density of states close to the band edge, we first assess the structural stability of the p-type material. The elastic energy ΔE_{el} is calculated as a function of the strain components ε_{xx} and ε_{yy} varying the lattice constants in x and y direction, and relaxing the internal

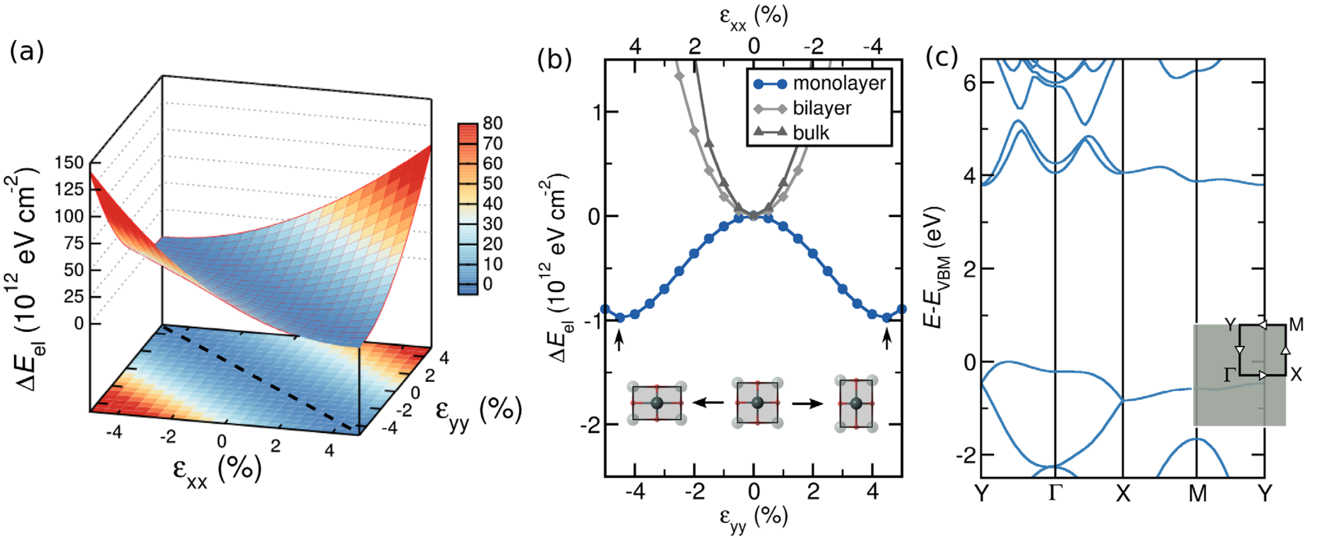

FIG. 3. Ferroelasticity in a α-SnO monolayer. (a) Elastic energy as a function of biaxial strain (ε_{xx} and ε_{yy}) in a α-SnO monolayer. The antisymmetric diagonal strain ($\varepsilon_{yy} = -\varepsilon_{xx}$) is shown in dashed black line. (b) Elastic energies of a α-SnO monolayer, bilayer, and bulk as a function of antisymmetric diagonal strain. Inset: α-SnO unit cells with schematic representation of the antisymmetric diagonal strains. (c) Electronic band structure of distorted α-SnO with $\varepsilon_{xx} = -\varepsilon_{yy} = 4.5$ % at HSE06 level.

coordinates. The surface $\Delta E_{\mathrm{el}}(\varepsilon_{xx}, \varepsilon_{yy})$ shown in Fig. 3(a) has two degenerate minima in $(+4.5\%, -4.5\%)$ and $(-4.5\%, +4.5\%)$, being characteristic of ferroelasticity. The two minima can be better seen in the transverse section $\varepsilon_{xx} = -\varepsilon_{yy}$ shown in Fig. 3(b). In contrast, the α-SnO bilayer and bulk only have a minimum at $\varepsilon_{xx} = \varepsilon_{yy} = 0$. Thus, only the α-SnO monolayer has FE order with intrinsic strain $\varepsilon_{xx} = -\varepsilon_{yy} = \pm 4.5\%$. This FE order breaks the point symmetry from C_{4v} to C_{2v}. At the minimum energy, the band structure of the α-SnO monolayer changes to have two valleys (between Γ and Y, and between Γ and $-Y$), see Fig. 3(c). The DOS of α-SnO with C_{4v} symmetry, C_{2v} symmetry, and α-SnO bilayer is given in the Supplemental Material [14].

Other electronic instability driven by the exchange interaction can be observed when we dope the α-SnO with holes. Increasing the hole density in monolayers leads to magnetization. This minimizes the magnetic energy, ΔE_{mag}, which we define as the difference between the paramagnetic and ferromagnetic systems. Positive values in Fig. 4(a) of ΔE_{mag} indicate the preference for the ferromagnetic order. Both square and distorted monolayers demonstrate magnetization up to $p = 6 \times 10^{14}$ cm^{-2}, the square monolayers being more stable at $p = 3.46 \times 10^{14}$ cm^{-2}. The α-SnO bilayer is only able to stabilize FM at higher hole densities, when the Fermi level reaches other peaks in the density of states. The magnetic dipole moment that arises in a p-doped α-SnO monolayer increases linearly with p, so that the ratio of the magnetic dipole and holes is close to 1 μ_B/holes up to 5×10^{14} cm^{-2}, as shown in Fig. 4(b). In the case $p = 3.46 \times 10^{14}$ cm^{-2}, we observe that the FM α-SnO monolayer is a half-metal phase wherein the spin up peaks in the DOS are filled, while the spin down peaks are empty, as shown in the Supplemental Material [14].

In order to show that FM order can be achieved in any 2D material with MHBEs, we construct a general model based on the Mexican-hat–like single band. This model can be applied to α-SnO monolayers, as well as to other materials with MHBEs, such as GaS [3] and GaSe [2] monolayers.

The model is based on the kinetic and exchange energies for systems with ferromagnetic and paramagnetic (PM) order. From these energies, we can obtain the energy difference between fully spin-polarized and unpolarized systems (see the Supplemental Material [14] for details):

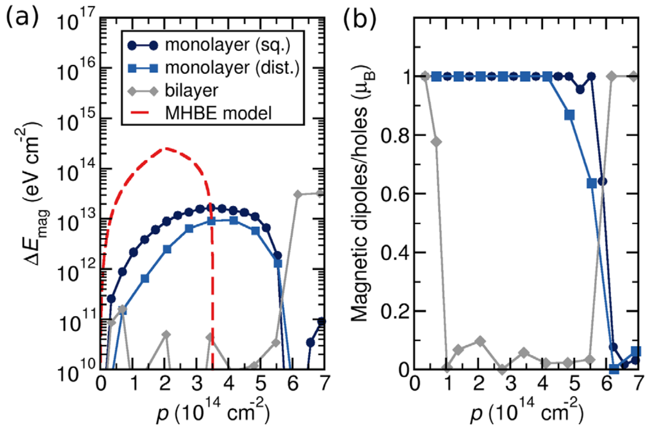

FIG. 4. Ferromagnetism in α-SnO. (a) Difference of energies between PM and FM orders as a function of hole density. First principles calculations and MHBE model (red). (b) Magnetic dipoles per holes as a function of hole density.

$$\Delta E_{\text{mag}} = p^2\left\{\pi^2 Ap - \frac{e^2}{2}\sqrt{\frac{-A}{2B}}\left[3 + 2\ln\left(\frac{-B}{Ap\pi}\right)\right]\right\}. \tag{3}$$

The A and B constants can be extracted from DFT, or fitted from experiments. The magnetic energy calculated with this model is also shown in Fig. 4(a). While the first-principles calculations show a maximal FM stability at $p \approx 3.5 \times 10^{14}$ cm^{-2} and FM-PM transition at $p \approx 6 \times 10^{14}$ cm^{-2}, the effective model shows the maximal FM stability at $p \approx 2 \times 10^{14}$ cm^{-2} and $p \approx 3.5 \times 10^{14}$ cm^{-2}.

In addition to FE and FM orders in the α-SnO monolayers, we can also observe phases where both orders are stabilized simultaneously. This regime, designated multiferroic (MF), is usually found in three-dimensional materials with perovskite structures, such as BiFeO$_3$ or BaTiO$_3$ [36,37] (with ferroelectricity, rather than ferroelasticity). However, so far, MF order has been found for no other 2D material. Varying the antisymmetric diagonal strain ($\varepsilon_{xx} = -\varepsilon_{yy}$) for p-doped α-SnO monolayers, we observe that some systems with low hole densities (0.69×10^{14} cm^{-2} and 2.07×10^{14} cm^{-2}) reveal FE with intrinsic strains $\varepsilon_{xx} = 6.0\%$ and $\varepsilon_{xx} = 5.5\%$. For the hole density $p = 3.46 \times 10^{14}$ cm^{-2}, the system is paraelastic (no nonzero intrinsic strain). The free energy densities for these systems doped with holes are shown in Fig. 5(a). Meanwhile, calculating the remanent magnetization (M_r) for these systems as function of strain, we observe that systems doped with holes up to $p = 1.38 \times 10^{14}$ cm^{-2} stabilize with FE order, but not with FM. For hole densities from 2.07×10^{14} cm^{-2} to 2.76×10^{14} cm^{-2}, both FE and FM are stable. Finally, for hole densities greater than 3.46×10^{14} cm^{-2}, only FM orders are stable. The remanent magnetization as functions of strain is shown in Fig. 5(b) for several values of hole densities. The maximum remanent magnetization found was $\mu_0 M_r = 135$ mT at $p = 5.54 \times 10^{14}$ cm^{-2}. The configurations of magnetization and strain that minimize the energies are shown in Fig. 5(b).

The phase transitions in these MF 2D materials can be described by a generalized Landau theory in which the free energy density is written as

$$F = \alpha(p)M^2 + \beta M^4 + \gamma\varepsilon^2 M^2 + \eta(p)\varepsilon^2 + \lambda\varepsilon^4, \tag{4}$$

where β, γ, and λ are positive constants. The functions $\alpha(p)$ and $\eta(p)$ can change the sign within the hole density range, leading to phase transitions. Close to these phase transitions, the functions are given by $\alpha(p) = \alpha_0(p_{c1} - p)$ and $\eta(p) = \eta_0(p - p_{c2})$, where α_0, η_0 are positive constants, and p_{c1} and p_{c2} are the critical hole densities for FM and FE, respectively. Fixing the magnetization to zero, the phase transitions from ferroelastic to paraelastic (PE) occurs at $p = p_{c2}$. The remaining three terms in free energy involving magnetization, create a phase transition at $\varepsilon_{pt} = \sqrt{\alpha_0(p - p_{c1})/\gamma}$. At higher strains and higher hole densities, the system is nonferroic (NF). Therefore, the physical condition for the multiferroic order to take place in a 2D material is $p_{c1} < p_{c2}$, as shown in Fig. 5(c). If $p_{c1} > p_{c2}$, the FE and FM will not exist at the same time. For the record, first principles results for α-SnO monolayers provide $p_{c1} \approx 2.1 \times 10^{14}$ cm^{-2} and $p_{c2} \approx 6.2 \times 10^{14}$ cm^{-2}, agreeing with the generalized Landau theory.

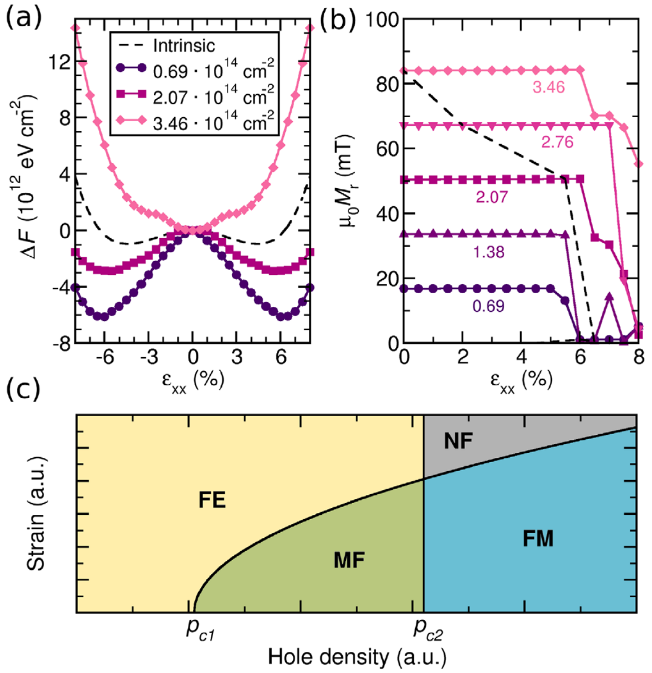

FIG. 5. Multiferroic phases in a α-SnO monolayer and models. (a) Free energy density as a function of the strain ε_{xx} for intrinsic and p-doped α-SnO. (b) Magnetization as a function of the strain ε_{xx}. Each curve is labeled by the hole density in 10^{14} cm^{-2}. The black dashed line shows the minimum energy strain. (c) Schematic phase diagram based on the generalized Landau model for multiferroicity (ferroelasticity and ferromagnetism) in a α-SnO monolayer.

In conclusion, we show that the α-SnO monolayer can be ferromagnetic, ferroelastic, or even multiferroic, depending on the hole density. This ordering is driven by the $1/\sqrt{E}$ divergence in the density of states. From a single-band model with Mexican-hat dispersion, we demonstrate that the ferromagnetism can be induced in a range of hole densities. Furthermore, we present a generalized Landau model where ferromagnetism, ferroelasticity, and multiferroicity can be stabilized. Using first-principles calculations on α-SnO as a prototype, we calculate the hole density range of 2–3 $\times 10^{14}$ cm^{-2}. However, since the ferromagnetism is caused by the Mexican-hat band dispersion, we can infer that other 2D materials can also manifest this order. In other words, a novel class of multiferroic 2D systems can be stabilized, leading to spontaneous symmetry breaking and a nontrivial control of the magnetism and strain. Moreover, these materials offer new possibilities for developments of flexible memories, and integration with other flexible devices.

The authors acknowledge the National Research Foundation, Prime Minister Office, Singapore, under its Medium Sized Centre Programme and CRP award "*Novel 2D materials with tailored properties: Beyond graphene*" (R-144-000-295-281). The first-principles calculations were carried out at the Centre for Advanced 2D Materials and Graphene Research Centre high-performance computing facilities.

---

*leandro.seixas@mackenzie.br

[1] D. Wickramaratne, F. Zahid, and R. K. Lake, Electronic and thermoelectric properties of van der Waals materials with ring-shaped valence bands, J. Appl. Phys. **118**, 075101 (2015).

[2] T. Cao, Z. Li, and S. G. Louie, Tunable Magnetism and Half-Metallicity in Hole-Doped Monolayer GaSe, Phys. Rev. Lett. **114**, 236602 (2015).

[3] S. Wu, X. Dai, H. Yu, H. Fan, J. Hu, and W. Yao, Magnetisms in *p*-type monolayer gallium chalcogenides (GaS, GaSe).arXiv:1409.4733v2.

[4] E. V. Castro, K. S. Novoselov, S. V. Morozov, N. M. R. Peres, J. M. B. L. dos Santos, J. Nilsson, F. Guinea, A. K. Geim, and A. H. Castro Neto, Biased Bilayer Graphene: Semiconductor with a Gap Tunable by the Electric Field Effect, Phys. Rev. Lett. **99**, 216802 (2007).

[5] H. Min, B. Sahu, S. K. Banerjee, and A. H. MacDonald, *Ab initio* theory of gate induced gaps in graphene bilayers, Phys. Rev. B **75**, 155115 (2007).

[6] Y. Zhang, T.-T. Tang, C. Girit, Z. Hao, M. C. Martin, A. Zettl, M. F. Crommie, Y. R. Shen, and F. Wang, Direct observation of a wide tunable band gap in bilayer graphene, Nature (London) **459**, 820 (2009).

[7] B. Skinner, B. I. Shklovskii, and M. B. Voloshin, Bound state energy of a Coulomb impurity in gapped bilayer graphene, Phys. Rev. B **89**, 041405(R) (2014).

[8] A. Ramasubramaniam and D. Naveh, Mn-doped monolayer MoS_2: An atomically thin dilute magnetic semiconductor, Phys. Rev. B **87**, 195201 (2013).

[9] L. Seixas, A. Carvalho, and A. H. Castro Neto, Atomically thin dilute magnetism in Co-doped phosphorene, Phys. Rev. B **91**, 155138 (2015).

[10] Y.-W. Son, M. L. Cohen, and S. G. Louie, Half-metallic graphene nanorribons, Nature (London) **444**, 347 (2006).

[11] Y. Du, H. Liu, B. Xu, L. Sheng, J. Yin, C.-G. Duan, and X. Wan, Unexpected magnetic semiconductor behavior in zigzag phosphorene nanoribbons driven by half-filled one dimensional band, Sci. Rep. **5**, 8921 (2015).

[12] P. Tao, H. Guo, T. Yang, and Z. Zhang, Strain-induced magnetism in MoS_2 monolayer with defects, J. Appl. Phys. **115**, 054305 (2014).

[13] Y. Liu, F. Xu, Z. Zhang, E. S. Penev, and B. I. Yakobson, Two-dimensional mono-elemental semiconductor with electronically inactive defects: The case of phosphorus, Nano Lett. **14**, 782 (2014).

[14] See Supplemental Material at http://link.aps.org/supplemental/10.1103/PhysRevLett.116.206803 for comparisons of PBE, PBE-D2, optB86b-vdW lattice parameters with experimental data, and details of Eqs. (2) and (3), which includes the Refs. [15–19].

[15] J. P. Perdew, K. Burke, and M. Ernzerhof, Generalized Gradient Approximation Made Simple, Phys. Rev. Lett. **77**, 3865 (1996).

[16] J. Klimeš, D. R. Bowler, and A. Michaelides, Chemical accuracy for the van der Waals density functional, J. Phys. Condens. Matter **22**, 022201 (2010).

[17] J. Klimeš, D. R. Bowler, and A. Michaelides, Van der Waals density functionals applied to solids, Phys. Rev. B **83**, 195131 (2011).

[18] S. Grime, Semiempirical gga-type density functional constructed with a long-range dispersion correction, J. Comput. Chem. **27**, 1787 (2006).

[19] W. J. Moore Jr. and L. Pauling, The crystal structures of the tetragonal monoxides of lead, tin, palladium, and platinum, J. Am. Chem. Soc. **63**, 1392 (1941).

[20] P. Hohenberg and W. Kohn, Inhomogeneous electron gas, Phys. Rev. **136**, B864 (1964).

[21] W. Kohn and L. J. Sham, Self-consistent equations including exchange and correlation effects, Phys. Rev. **140**, A1133 (1965).

[22] G. Kresse and J. Furthmüller, Effecient itarative schemes for *ab initio* total-energy calculations using a plane-wave basis set, Phys. Rev. B **54**, 11169 (1996).

[23] G. Kresse and D. Joubert, From ultrasoft pseudopotentials to the projector augmented-wave method, Phys. Rev. B **59**, 1758 (1999).

[24] P. E. Blöchl, Projector augmented-wave method, Phys. Rev. B **50**, 17953 (1994).

[25] J. Heyd, G. E. Scuseria, and M. Ernzerhof, Hybrid functionals based on a screened Coulomb potential, J. Chem. Phys. **118**, 8207 (2003); **124**, 219906(E) (2006).

[26] H. J. Monkhorst and J. D. Pack, Special points for Brillouin-zone integrations, Phys. Rev. B **13**, 5188 (1976).

[27] A. K. Singh and R. G. Hennig, Computational prediction of two-dimensional group-IV monochalcogenides, Appl. Phys. Lett. **105**, 042103 (2014).

[28] M. Meyer, G. Onida, A. Ponchel, and L. Reining, Electronic structure of stannous oxide, Comput. Mater. Sci. **10**, 319 (1998).

[29] A. Walsh and G. W. Watson, Electronic structures of rocksalt, litharge, and herzenbergite SnO by density functional theory, Phys. Rev. B **70**, 235114 (2004).

[30] Y. W. Li, Y. Li, T. Cui, L. J. Zhang, Y. M. Ma, and G. T. Zou, The pressure-induced phase transition in SnO: a first-principles study, J. Phys. Condens. Matter **19**, 425230 (2007).

[31] J. P. Allen, D. O. Scanlon, S. C. Parker, and G. W. Watson, Tin monoxide: Structural prediction from first principles calculations with van der Waals corrections, J. Phys. Chem. C **115**, 19916 (2011).

[32] K. Govaerts, R. Saniz, B. Partoens, and D. Lameon, van der Waals bonding and the quasiparticle band structure of SnO from first principles, Phys. Rev. B **87**, 235210 (2013).

[33] A. Togo, F. Oba, I. Tanaka, and K. Tatsumi, First-principles calculations of native defects in tin monoxide, Phys. Rev. B **74**, 195128 (2006).

[34] D. K. Efetov and P. Kim, Controlling Electron-Phonon Interactions in Graphene at Ultrahigh Carrier Densities, Phys. Rev. Lett. **105**, 256805 (2010).

[35] L. J. Li, E. C. T. O' Farrel, K. P. Loh, B. Özyilmaz, and A. H. Castro Neto, Controlling many-body states by the electric-field effect in a two-dimensional material, Nature (London) **529**, 185 (2016).

[36] S.-C. Cheong and M. Mostovoy, Multiferroics: A magnetic twist for ferroelectricity, Nat. Mater. **6**, 13 (2007).

[37] D. Khomskii, Trend: Classifying multiferroics: Mechanisms and effects, Physics **2**, 20 (2009).